Incorporating the Effects of Moisture into a Dynamical Parameter: Moist Vorticity and Moist Divergence

WEIHONG QIAN

Department of Atmospheric and Oceanic Sciences, Peking University, Beijing, China

JUN DU

NOAA/NCEP/Environmental Modeling Center, College Park, Maryland

XIAOLONG SHAN AND NING JIANG

Department of Atmospheric and Oceanic Sciences, Peking University, Beijing, China

(Manuscript received 20 November 2014, in final form 21 April 2015)

ABSTRACT

Properly including moisture effects into a dynamical parameter can significantly increase the parameter's ability to diagnose heavy rain locations. The relative humidity–based weighting approach used to extend the moist potential vorticity (MPV) to the generalized moist potential vorticity (GMPV) is analyzed and demonstrates such an improvement. Following the same approach, two new diagnostic parameters, moist vorticity (MV) and moist divergence (MD), have been proposed in this study by incorporating moisture effects into the traditional vorticity and divergence. A regional heavy rain event that occurred along the Yangtze River on 1 July 1991 is used as a case study, and 41 daily regional heavy rain events during the notorious flooding year of 1998 in eastern China are used for a systematic evaluation. Results show that after the moisture effects were properly incorporated, the improved ability of all three parameters to capture a heavy rain area is significant (statistically at the 99% confidence level): the GMPV is improved over the MPV by 194%, the MD over the divergence by 60%, and the MV over the vorticity by 34% in terms of the threat score (TS). The average TS is 0.270 for the MD, 0.262 for the MV, and 0.188 for the GMPV. Application of the MV and MD to assess heavy rain potential is not intended to replace a complete, multiscale forecasting methodology; however, the results from this study suggest that the MV and MD could be used to postprocess a model forecast to potentially improve heavy rain location predictions.

1. Introduction

There are many diagnostic parameters developed in meteorology to diagnose or predict various weather elements in short-range (from hours to a few days) forecasts, such as convective available potential energy (CAPE) for convection (Moncrieff and Miller 1976), Haines index for fire weather (Haines 1988), the fog-diagnostic scheme (Zhou and Du 2010), and the icing scheme for aviation weather (S. Silberberg 2014, personal communication). For long-range forecasts, there is the monsoon index (Wang and Fan 1999), El Niño–Southern Oscillation (ENSO) index (Wolter and Timlin 1993), Madden–Julian oscillation (MJO) index (Ventrice et al. 2013; Kiladis et al. 2014), and North Atlantic Oscillation (NAO) index (Hurrell 1995). In this study we will propose two new parameters, moist vorticity and moist divergence, for diagnosing heavy rain locations.

Heavy rain is an outcome of combined favorable dynamic and moisture conditions. It has been shown that combining dynamic and moisture factors together in a forecast method can greatly improve heavy rain prediction [e.g., Doswell et al. (1996), where precipitation efficiency and duration are another two important elements considered in their method]. The extension of potential vorticity (PV) to moist potential vorticity (MPV) is an example of combining dynamic and moisture factors (Bennetts and Hoskins 1979). Another example is the generalization of the MPV, that is, generalized moist

Corresponding author address: Prof. Weihong Qian, Dept. of Atmospheric and Oceanic Sciences, Peking University, Beijing 100871, China.
E-mail: qianwh@pku.edu.cn

DOI: 10.1175/WAF-D-14-00154.1

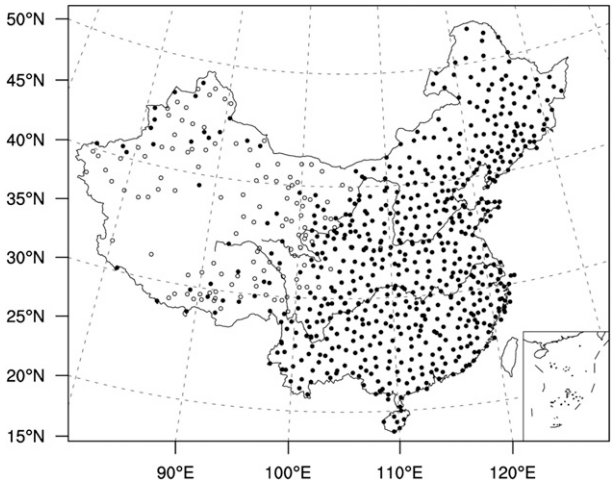

FIG. 1. Distribution of 754 weather stations in China. Filled (open) circles indicate stations with (without) heavy rain days ($\geq$50 mm day^{-1}) from 1960 to 2010.

potential vorticity (GMPV; Gao et al. 2004a). Both the MPV and GMPV will be further explored in our study. How to properly include moisture effects into a dynamic factor is not obvious. We use this study to demonstrate a feasible way to include moisture effects within a dynamical parameter and how this inclusion improves the parameter's performance through a case study and systematic evaluation. The goal of this study is not to suggest that the application of this parameter can replace a conceptual model–based, multiscale forecast process, but simply to demonstrate how the incorporation of moisture effects in the parameter can improve the correlation between areal coverage of the parameter and the observed rainfall location. In the study, a regional heavy rain event that occurred on 1 July 1991 is used for a detailed analysis and method test. An independent dataset of 41 daily regional heavy rain cases from the notorious flooding year of 1998 in eastern China is used for a systematic evaluation to confirm the robustness of our approach. In the rest of this paper, the datasets and the heavy rain cases will be described in section 2, the results are presented in section 3, and a summary and discussion are provided in section 4.

2. Dataset and case description

Two datasets are used in this study. The first one is the observed precipitation from 754 weather stations across mainland China (Fig. 1). The stations are relatively uniformly spaced throughout eastern China and more sparsely distributed across western China. Most stations in eastern China are located in the East Asian monsoon region and experienced at least 1 day of heavy rain (filled circles) during the period 1960–2010. A daily local heavy rain (LHR) event is defined when the precipitation amount accumulated over a 24-h period (from 1200 UTC to 1200 UTC on the following day) exceeds 50 mm at a station. When two or more adjacent stations (less than 200 km apart) meet the LRH criteria at the same time, a daily regional heavy rain (RHR) event is defined. The term heavy rain used in this study refers to a daily RHR event. These observed precipitation data are interpolated onto a 0.5° latitude–longitude grid using the ordinary Kriging method of Chen et al. (2010), which is used for the threat score (TS) calculation in section 3. The second dataset is the European Centre for Medium-Range Weather Forecasts (ECMWF) interim reanalysis (ERA-Interim), which is used for calculating various diagnostic parameters. The ERA-Interim is on a 0.75° (~80 km) latitude–longitude grid with standard pressure levels from 1000 to 50 hPa (Dee et al. 2011). This dataset is available online (http://apps.ecmwf.int/datasets/data/interim-full-daily). Given that the ERA-Interim is about 0 km in spatial resolution, only long-lasting (24 h) large-scale widespread regional heavy rain events (more than 10 adjacent stations with observed rainfall exceeding 50 mm day^{-1}) caused by obvious synoptic-scale circulation systems (Qian 2013) are used in this study (see Table 1), while those isolated local heavy rain events probably caused by individual convective systems are excluded.

From 30 June to 12 July 1991, a prolonged heavy rain event occurred over the lower Yangtze River basin, in response to a series of short waves moving eastward across the area (Ding 1993). On 1 July 1991, 22 stations exceeded 50 mm day^{-1} of rainfall with a precipitation maximum of 201.8 mm day^{-1} and an average precipitation total of 96.5 mm day^{-1}. The event on 1 July (from 1200 UTC 30 June to 1200 UTC 1 July) is showcased in this study. During the summer of 1998, heavy rain events frequently occurred over the Yangtze River basin, resulting in the most severe flooding on record and leading to the deaths of more than 3000 people. Direct economic losses of about CNY 167 billion [equivalent to about $28 billion (U.S. dollars)] were associated with the flooding (National Climate Center of China 1998). There were 41 daily regional heavy rain episodes during that summer based on the criterion of having at least 10 adjacent stations exceeding 50 mm day^{-1} (a 24-h period centered at 0000 UTC of a day) rainfall at each station. These 41 cases are listed in Table 1 with a brief description including the date and number of stations with precipitation exceeding 25, 50, or 100 mm day^{-1}, as well as associated synoptic-scale systems. On 7 July 1998, there were two regional heavy rain events over northwestern and northeastern

TABLE 1. Description of the 41 daily regional heavy rain events that occurred in eastern China in 1998.

Date	No. of sites with rainfall ≥(25/50/100) mm day^{-1}	Region	Synoptic-scale system	Date	No. of sites with rainfall ≥(25/50/100) mm day^{-1}	Region	Synoptic-scale system
14 Jan	68/23/0	Southern Yangtze River	Cyclone	1 Jul	18/10/2	Northern China	Cyclone
16 Feb	24/10/0	Southern Yangtze River	Reversed trough	2 Jul	43/23/5	Northern China	Cyclone
17 Feb	31/10/0	Southern China	Reversed trough	3 Jul	26/12/0	Yangtze River	Shear
8 Mar	45/13/0	Southern Yangtze River	Reversed trough	6 Jul	29/12/1	Northeastern China	Cyclone
9 Mar	43/16/0	Southern China	Cyclone	7 Jul	15/11/0	Northwestern China	Cyclone
11 Apr	52/11/2	Yangtze River	Cyclone	7 Jul	24/10/2	Northeastern China	Cyclone
2 May	54/14/1	Yangtze River	Shear	8 Jul	21/10/2	Northeastern China	Cyclone
14 May	36/15/5	Southern Yangtze River	Cyclone	13 Jul	31/14/3	Northeastern China	Cyclone
22 May	24/10/1	Southwestern China	Reversed trough	14 Jul	32/14/1	Northeastern China	Cyclone
23 May	45/14/4	Yangtze River	Cyclone	15 Jul	17/11/0	Northeastern China	Cyclone
9 Jun	34/11/2	Southern coast	Shear	22 Jul	16/11/4	Yangtze River	Shear
12 Jun	29/11/1	Yangtze River	Cyclone	23 Jul	42/22/5	Yangtze River	Cyclone
13 Jun	24/16/9	Yangtze River	Shear	24 Jul	39/15/3	Southern Yangtze River	Cyclone
14 Jun	30/17/7	Southern Yangtze River	Shear	29 Jul	26/14/3	Southern Yangtze River	Cyclone
19 Jun	70/36/6	Yangtze River	Shear	30 Jul	28/12/3	Yangtze River	Cyclone
21 Jun	45/17/5	Southern Yangtze River	Shear	4 Aug	34/18/7	Northern China	Cyclone
23 Jun	62/22/3	Yangtze River	Shear	5 Aug	42/22/2	Northeastern China	Cyclone
24 Jun	70/37/10	Southern Yangtze River	Reversed trough	7 Aug	24/11/1	Northern China	Cyclone
25 Jun	57/25/5	Yangtze River	Shear	15 Aug	28/13/0	Northern China	Cyclone
26 Jun	35/21/3	Yangtze River	Shear	22 Aug	23/12/2	Northern China	Cyclone
30 Jun	16/10/2	Yangtze River	Cyclone	27 Aug	22/11/1	Yangtze River	Shear

China. Among these 41 cases, most of them occurred along or south of the Yangtze River. They were mainly associated with the synoptic-scale frontal boundary (horizontal wind shear, convergence zone, and reversed trough) and extratropical cyclones (Table 1). These 41 cases are used for systematic evaluation in this study.

3. Dynamic and moisture parameters in diagnosing heavy rain

a. Vorticity, divergence, and relative humidity

Equations (1) and (2) are the relative vorticity ζ and horizontal divergence D expressed in the form of planar coordinates:

$$\zeta = \left(\frac{\partial v}{\partial x} - \frac{\partial u}{\partial y}\right) \quad \text{and} \tag{1}$$

$$D = \left(\frac{\partial u}{\partial x} + \frac{\partial v}{\partial y}\right). \tag{2}$$

Since heavy precipitation is closely associated with convergent and cyclonic flows in a moist environment, either dynamic or moisture factors alone should not be able to accurately depict the area of a heavy rain event. Figures 2 and 3 show the relative vorticity [Eq. (1)] and divergence [Eq. (2)] at 850 hPa at every 6 h during the entire period (from 1200 UTC 30 June to 1200 UTC 1 July) of the 1 July 1991 heavy rain event. Although they are generally similar to each other at different times during the event, the midpoint, 0000 UTC (Figs. 2c, 3c), seems to match the heavy rain area the best (at least as well as others). Therefore, the midpoint will be used as a representative time hereafter in this study. In Figs. 2 and 3, there are two main areas of maximal positive vorticity (cyclonic flow) and negative divergence (convergence): one in southern China along the Yangtze River and another in northwestern China around 40°N. The former coincides well with the heavy rainband, while the latter does not correspond to any precipitation band (because of a lack of favorable moisture conditions). Figure 4 shows the relative humidity at 850 hPa at 0000 UTC

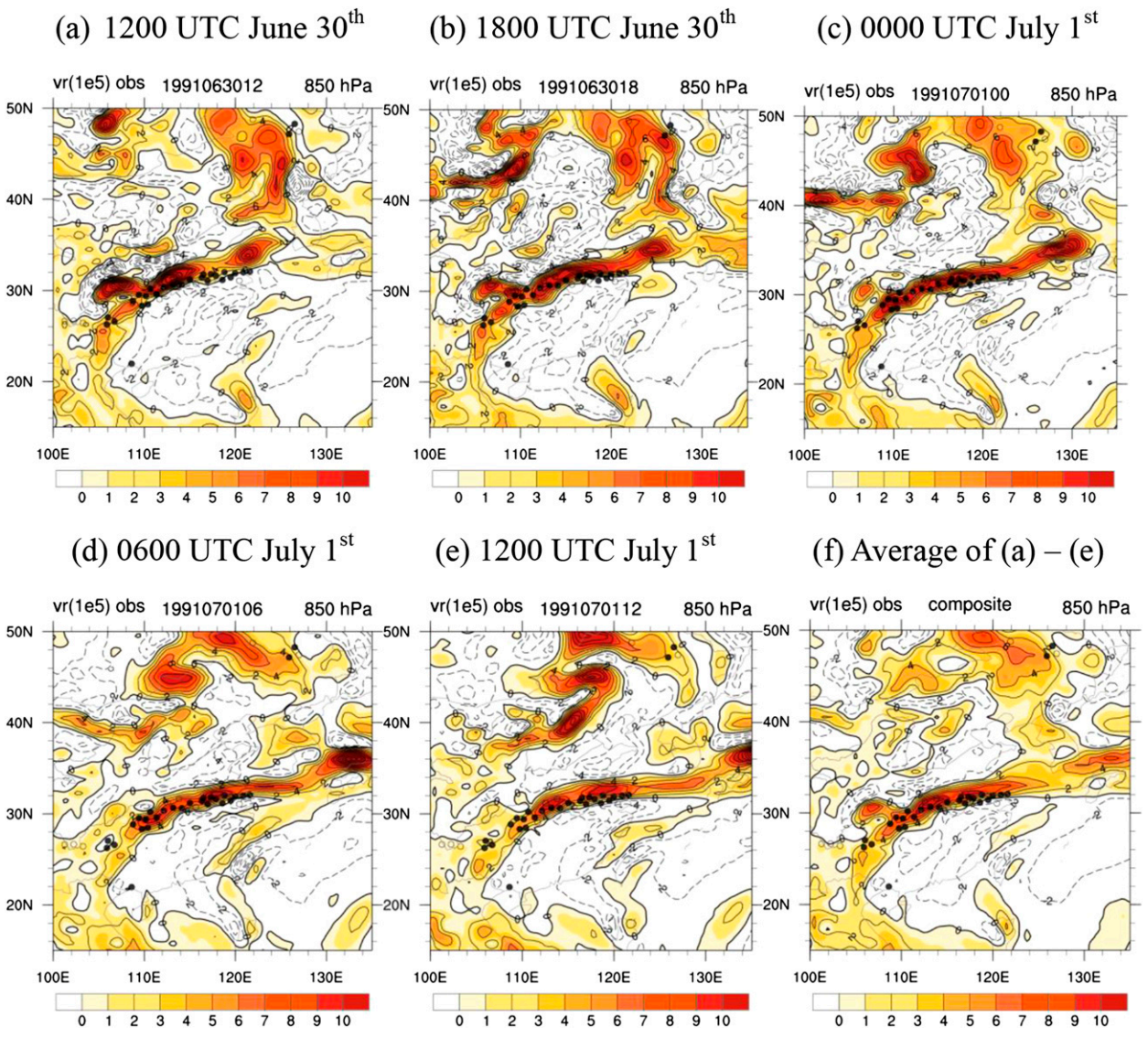

FIG. 2. Horizontal distribution of vorticity at 850 hPa (s^{-1}; contours with an interval of 2×10^{-5} s^{-1}) at (a) 1200 and (b) 1800 UTC 30 Jun and at (c) 0000, (d) 0600, and (e) 1200 UTC 1 Jul 1991; (f) the average of (a)–(e). Filled (open) circles indicate the stations with rainfall exceeding 50 (25–50) mm during the 24-h period from 1200 UTC 30 Jun to 1200 UTC 1 Jul 1991.

1 July 1991. The heavy rainband along the Yangtze River coincides well with a maximum relative humidity area, while the maximum relative humidity area in southwestern China does not correspond to any precipitation band (because of a lack of favorable dynamic conditions). Figures 2–4 demonstrate that although a dynamic or moisture parameter alone can reflect heavy rain regions it also exhibits false alarm regions. Physically, it is implied that heavy rain requires both forcing for ascent and moisture to be coincident across a same area. Therefore, parameters with both dynamic and moisture factors combined are needed to hopefully depict heavy rain areas more exclusively.

b. Moist potential vorticity and generalized MPV

How do we properly include moisture effects in a dynamical parameter? PV is used as an example in this section. PV is a dynamical diagnostic parameter and can be derived from the combination of the first law of thermodynamics and the law of momentum conservation, which implies that PV can only be changed by diabatic heating or frictional processes. Equation (3) gives the PV expression commonly used in meteorology:

$$\mathrm{PV} = \rho^{-1}\zeta_a \nabla\theta \quad \text{and} \tag{3}$$

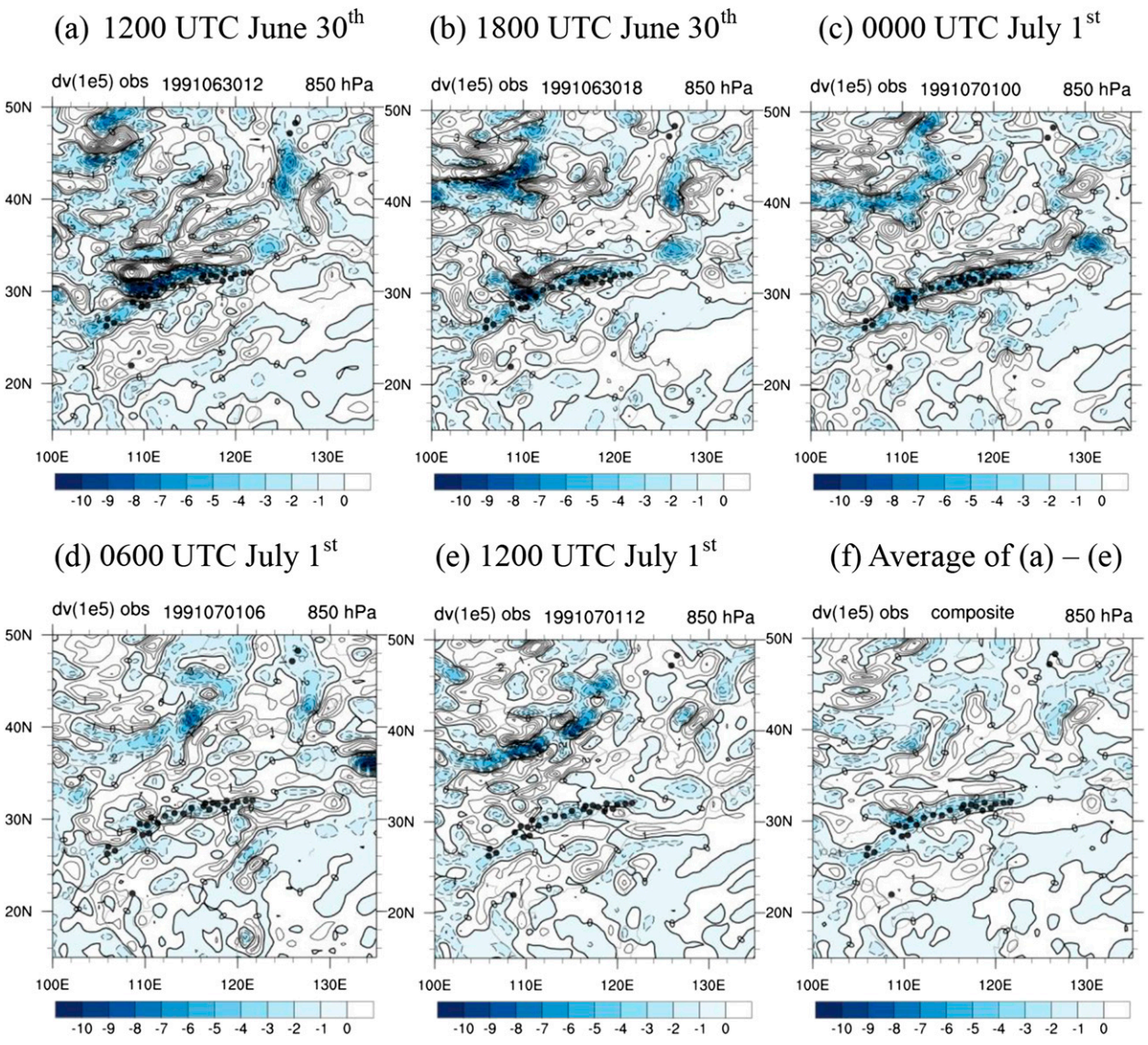

FIG. 3. As in Fig. 2, but for divergence at 850 hPa (s^{-1}; contours with an interval of $1 \times 10^{-5}\,s^{-1}$).

$$\zeta_a = f + \zeta = 2\Omega \sin\varphi + \left(\frac{\partial v}{\partial x} - \frac{\partial u}{\partial y}\right), \tag{4}$$

where f is the Coriolis parameter, Ω is the angular speed of Earth's rotation, φ is Earth's geographical latitude, ρ is the fluid (air) density, ζ_a is the absolute vorticity [Eq. (4)], and θ is the potential temperature. PV is often used to diagnose observed atmospheric behavior and to understand synoptic-scale dynamics and atmospheric numerical simulation results (Cao and Cho 1995; Shou and Li 1999; Schubert et al. 2001; Gao et al. 2004a,b; Deng and Gao 2009). Since PV is not conserved when latent heat release is taken into account in a saturated moist atmosphere, Bennetts and Hoskins (1979) first generalized PV into MPV by replacing θ with the equivalent potential temperature θ_e in the PV equation; that is,

$$\mathrm{MPV} = \rho^{-1}\zeta_a \nabla\theta_e. \tag{5a}$$

Schubert et al. (2001) proved an annihilation of the solenoidal term in the MPV equation, thus leading to a conservation of MPV in moist-adiabatic and frictionless processes. The MPV at a pressure coordinate consists of two terms, MPV1 and MPV2:

$$\mathrm{MPV1} = -g(\zeta + f)\frac{\partial\theta_e}{\partial p} = -g\left[\left(\frac{\partial v}{\partial x} - \frac{\partial u}{\partial y}\right) + f\right]\frac{\partial\theta_e}{\partial p} \quad \text{and} \tag{5b}$$

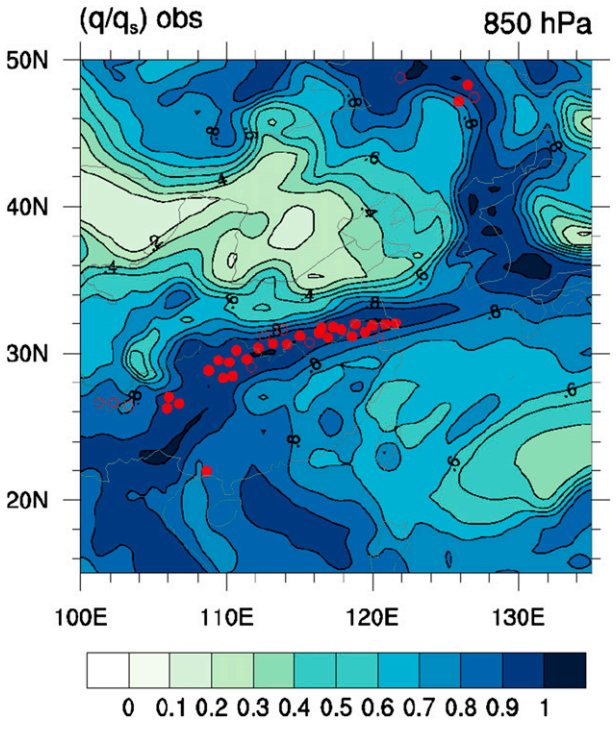

FIG. 4. Horizontal distribution of relative humidity (q/q_s) at 850 hPa (unitless; contours with an interval of 0.1) at 0000 UTC 1 Jul 1991. Filled (open) circles indicate the stations with rainfall exceeding 50 (25–50) mm during the 24-h period from 1200 UTC 30 Jun to 1200 UTC 1 Jul 1991.

$$\mathrm{MPV2} = g\left[\left(\frac{\partial v}{\partial p}\right)\left(\frac{\partial \theta_e}{\partial x}\right) - \left(\frac{\partial u}{\partial p}\right)\left(\frac{\partial \theta_e}{\partial y}\right)\right], \tag{5c}$$

where p is air pressure and g is Earth's gravitational force. MPV1 is a product of absolute vorticity (related to ascent) and the vertical gradient of equivalent potential temperature (related to atmospheric instability) and represents the impact of convective instability on vorticity growth; MPV2 is a product of vertical wind shear and the horizontal gradient of equivalent potential temperature and represents the impact of vertical wind shear and baroclinicity on vorticity development (Wu et al. 1995).

MPV has been extensively used in studies of conditional symmetric instability (Emanuel 1983, 1988; Bennetts and Sharp 1982; Schultz and Schumacher 1999) and the generation of MPV in extratropical cyclones (Cao and Cho 1995; Martínez-Alvarado et al. 2010). MPV has also been used in the analysis of heavy rainfall (Shou and Li 1999; Clark et al. 2002; Gao et al. 2004a,b; Deng and Gao 2009; Novak et al. 2009; Zhou et al. 2010). Gao et al. (2004b) argued that maximum MPV and maximum surface rainfall are nearly collocated as a result of the impact of heat and mass forcing on the development of MPV and argued that MPV can, therefore, be used to track the propagation of rain systems (see their Figs. 1–4). However, there is only one case visually examined in Gao et al. (2004b). In this study, we will systematically and quantitatively examine the performance of MPV in diagnosing heavy rain locations. Figure 5 shows the vertical cross section of MPV along with its two components (MPV1 and MPV2) for the 1 July 1991 regional heavy rain case. MPV has virtually no ability to depict a heavy rain area (Fig. 5a) because of the opposite signals coming from the MPV1 (Fig. 5b) and MPV2 (Fig. 5c) over the heavy rain region. The two components can depict the heavy rain location better than MPV can itself (e.g., the maximal axes of positive MPV1 and negative MPV2 extend to the lower level right over the heavy rainband). To examine their horizontal distribution, Fig. 6 shows the MPV and its two components at 850 and 925 hPa. Consistent with Fig. 5, the MPV (Figs. 6a,d) does not match the heavy rain area because of the opposite signs of the two components. Although the MPV1 (Figs. 6b,e) does cover most or at least part of the heavy rain area, it is too widespread spatially, resulting

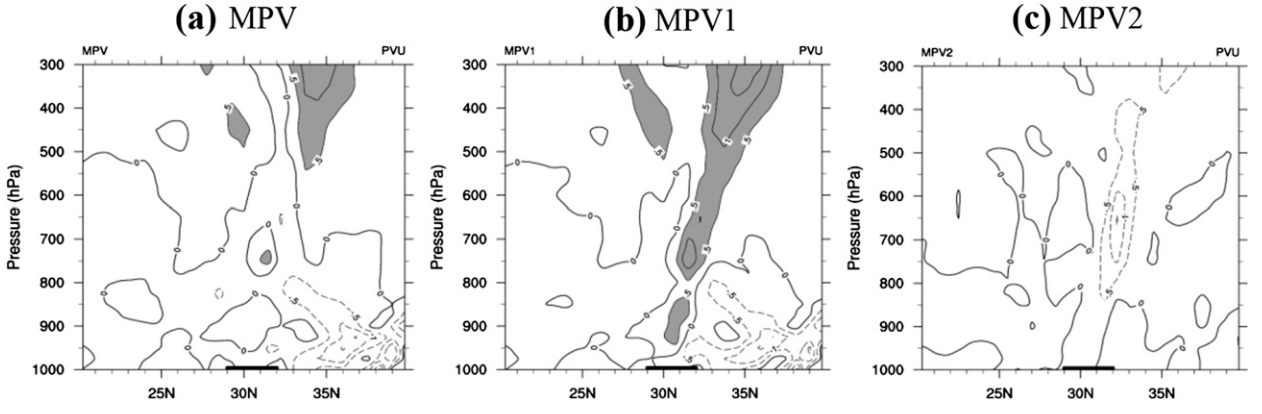

FIG. 5. Vertical–latitude cross sections of (a) MPV, (b) MPV1, and (c) MPV2 [potential vorticity units (PVU); where 1 PVU = 10^{-6} K kg^{-1} m^2 s^{-1}; contours with an interval of 0.5 PVU] along 114.75°E at 0000 UTC 1 Jul 1991. The thick horizontal line at the surface represents the area of heavy rain. The shading indicates positive PV with values larger than 0.5 PVU.

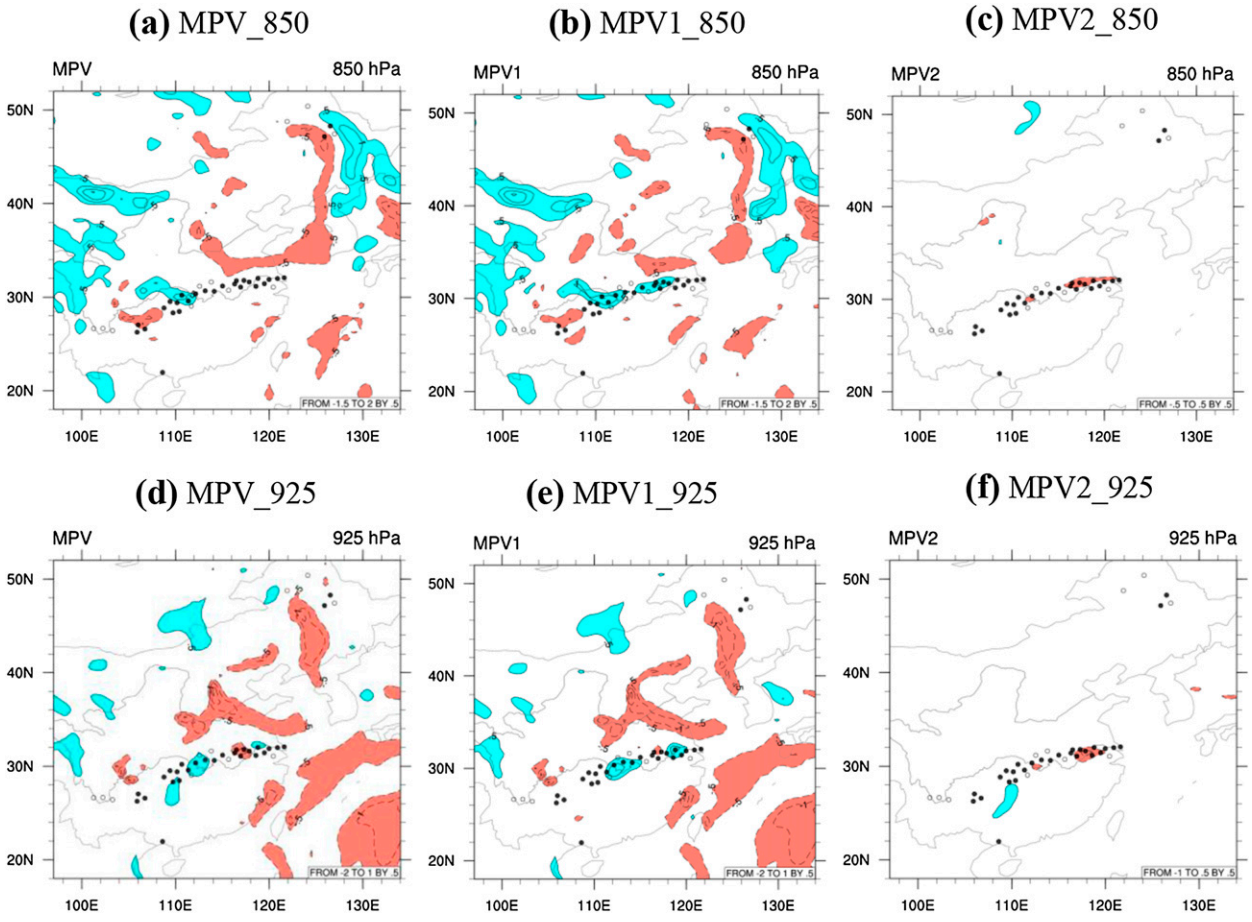

FIG. 6. (a) MPV, (b) MPV1, and (c) MPV2 at 850 hPa (contours with an interval of 0.5 PVU) at 0000 UTC 1 Jul 1991. (d)–(f) As in (a)–(c), but for 925 hPa. Filled (open) circles indicate the stations with rainfall exceeding 50 (25–50) mm day^{-1}. Positive (negative) PV is shown by solid (dashed) lines, where cyan (brown) shading covers values >0.5 PVU (<−0.5 PVU).

in a high false alarm rate. The MPV2 (Figs. 6c,f) is the best among the three with much reduced false alarms but misses many heavy rain spots such as the heavy rainband in the western end of the Yangtze River and the heavy rain area in northeastern China because of a lack of coverage. For the MPV, MPV1, and MPV2, their performance is better at 850 than 925 hPa. Therefore, they will be evaluated at 850 hPa hereafter.

To improve the capability of the MPV in depicting heavy rain locations, Gao et al. (2004a) proposed a generalized MPV by tweaking the moisture effects in the MPV. The rationale behind their modification is that in the real atmosphere an assumed generally saturated (if defined as 100% in relative humidity) air mass might not be uniformly saturated; for example, the relative humidity of lighter fog could be less than 100% and different from that of denser fog. To reflect this nonuniformity in the moisture conditions, Gao et al. (2004a) first defined a generalized equivalent potential temperature θ^* by multiplying a relative humidity (q/q_s)-based weight (called the condensation probability function) in a formula for the equivalent potential temperature under saturated situations as follows:

$$\theta^* = \theta \exp\left[\frac{Lq_s}{c_p T}\left(\frac{q}{q_s}\right)^k\right], \tag{6}$$

where L is latent heat released from condensation by a unit air mass, c_p is the heat capacity of dry air held at a constant pressure, q is air specific humidity, q_s is air saturated specific humidity, T is air temperature, and k is an empirical constant varying from 1 to 20, representing an exponential power of relative humidity. If $k = 1$ or 0, it becomes the regular equivalent potential temperature of unsaturated or saturated air. This new definition distinguishes the relative contribution of saturated water vapor based on its moisture content. Furthermore, by replacing the equivalent potential temperature with the generalized equivalent potential temperature in Eq. (5a), the MPV can thus be extended to GMPV:

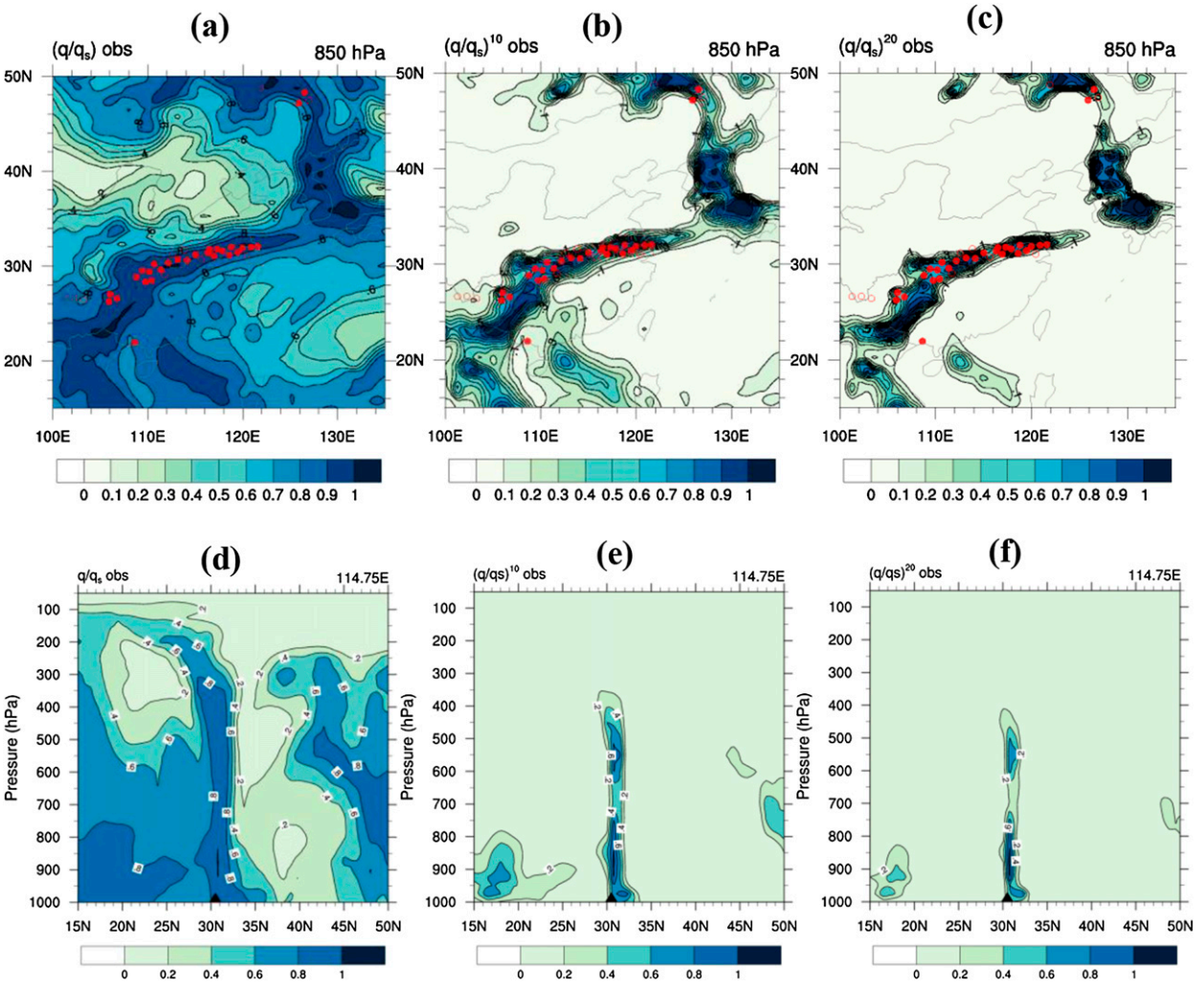

FIG. 7. Impact of k value on the relative humidity–based weight at 0000 UTC 1 Jul 1991: (a) $k = 1$, (b) $k = 10$, and (c) $k = 20$ for horizontal distribution (unitless; contours with an interval of 0.1) and (d) $k = 1$, (e) $k = 10$, and (f) $k = 20$ for vertical distribution (unitless; contours with an interval of 0.2). Filled (open) circles indicate the stations with rainfall exceeding 50 (25–50) mm day^{-1} in (a)–(c), and the heavy rain area is indicated by the filled triangles in (d)–(f).

$$\mathrm{GMPV} = \rho^{-1}\zeta_a \nabla\theta^*. \tag{7a}$$

If $k = 1$, it becomes the original MPV. A similar expression and application can also be found in Korty and Schneider (2007). Following Eqs. (5b) and (5c), the two components of the GMPV (GMPV1 and GMPV2) can be expressed as

$$\mathrm{GMPV1} = -g(\zeta + f)\frac{\partial\theta^*}{\partial p} = -g\left[\left(\frac{\partial v}{\partial x} - \frac{\partial u}{\partial y}\right) + f\right]\frac{\partial\theta^*}{\partial p} \quad \text{and} \tag{7b}$$

$$\mathrm{GMPV2} = g\left[\left(\frac{\partial v}{\partial p}\right)\left(\frac{\partial\theta^*}{\partial x}\right) - \left(\frac{\partial u}{\partial p}\right)\left(\frac{\partial\theta^*}{\partial y}\right)\right]. \tag{7c}$$

Similar to MPV1 and MPV2, GMPV1 is related to the impact of convective instability and GMPV2 is related to vertical wind shear and the horizontal distribution of heat and moisture (moist baroclinicity). It was reported that GMPV and its components have been applied to diagnoses of heavy rain in several previous studies (Gao et al. 2002, 2004b; Deng and Gao 2009; Zhou et al. 2010). Those studies used the maximum GMPV to trace heavy rain locations. But no systematic quantitative evaluation has been done in these studies. The k value controls the moisture impact area. When $k = 1$, the moisture impact spreads to the largest area, and when k increases, the moisture impact will be concentrated in a smaller area given $q/q_s \leq 1.0$. Figure 7 shows the impact of varying the k value on the relationship between relative humidity–based weight and heavy rainfall in plain view (Figs. 7a–c) and in vertical cross sections (Figs. 7d–f) for the 1 July 1991 case. We can see that the impact area is

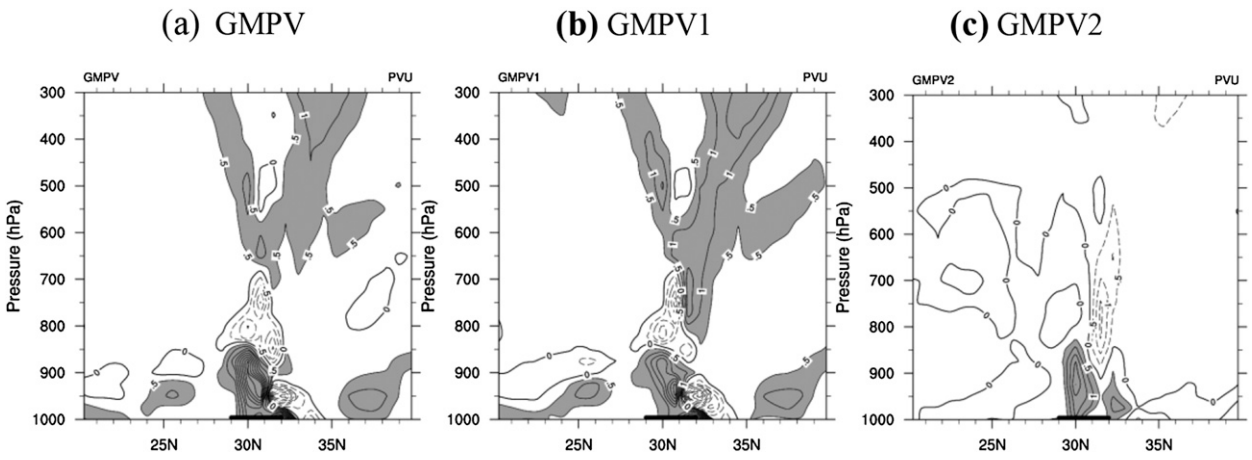

FIG. 8. As in Fig. 5, but for (a) GMPV, (b) GMPV1, and (c) GMPV2 ($k = 10$).

too wide when $k = 1$, that it misses some heavy rain spots when $k = 20$ (e.g., Fig. 7c), and that it covers all the heavy rain spots when $k = 10$. Therefore, $k = 10$ is used throughout this study. To examine if GMPV is superior to MPV in diagnosing heavy rain locations, Fig. 8 shows the vertical–latitude cross section of the GMPV along with its two components for the 1 July 1991 case. Comparing Fig. 8 with Fig. 5, the improvement found in GMPV (Fig. 8a) over MPV (Fig. 5a) is obvious. Not only the two components (Figs. 8b,c) but the GMPV itself

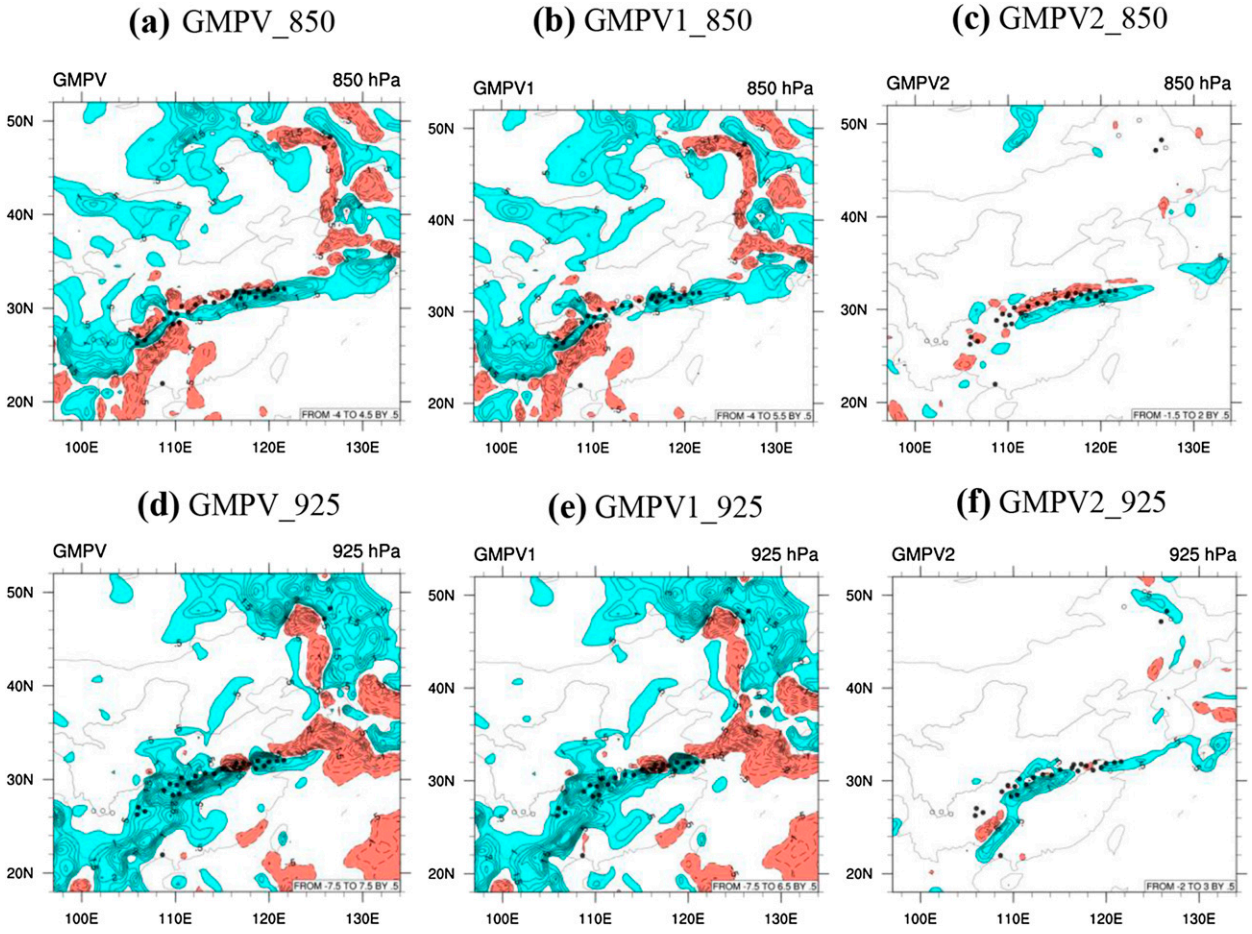

FIG. 9. As in Fig. 6, but for (a),(d) GMPV; (b),(e) GMPV1; and (c),(f) GMPV2 ($k = 10$).

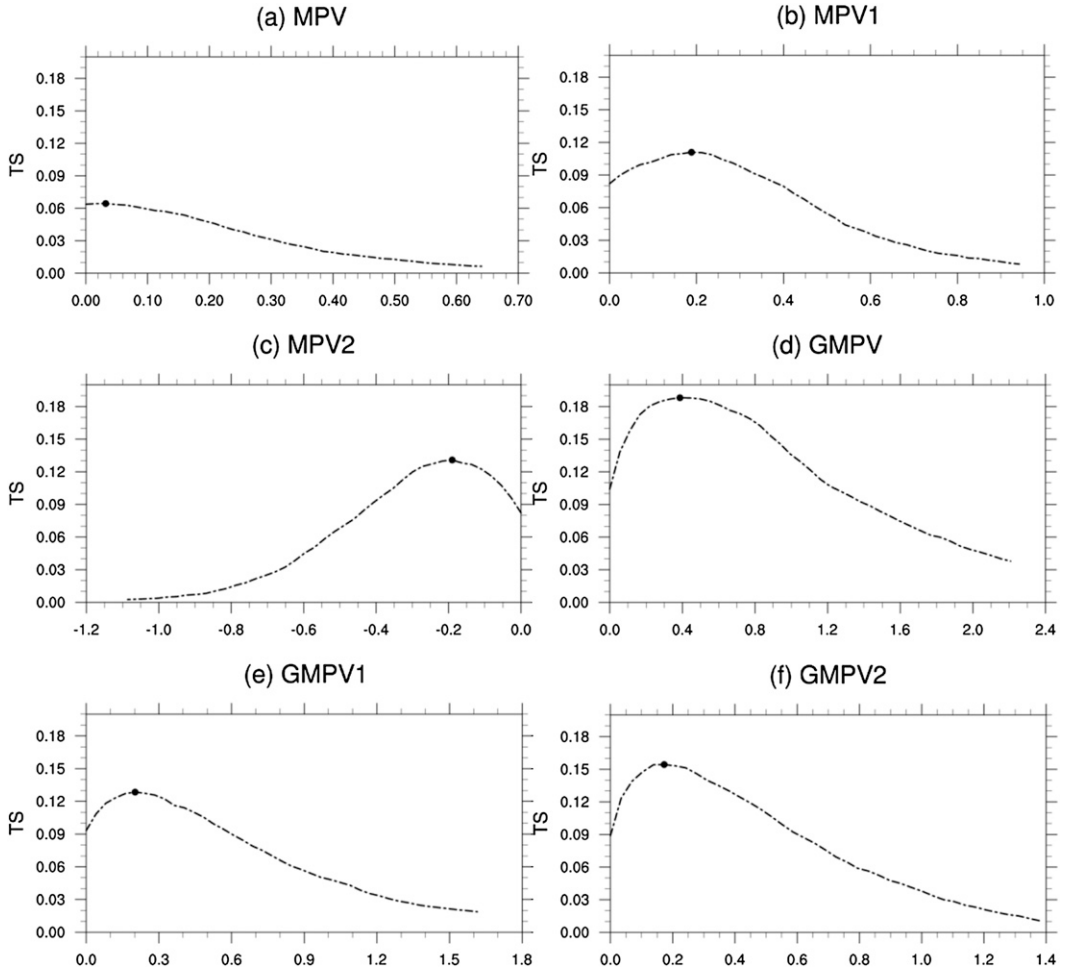

FIG. 10. Variation of TS with the threshold of parameters, averaged over the 41 daily heavy rain cases occurring in eastern China during 1998. The black dots correspond to the optimal thresholds for (a) MPV, (b) MPV1, (c) MPV2, (d) GMPV, (e) GMPV1, and (f) GMPV2, respectively.

(Fig. 8a) now has a clear strong signal pointing to the heavy rain location because the two components have the same sign in the GMPV, while there is no clear signal in the MPV (Fig. 5a). Unlike the MPV, the strongest signals from the GMPV are concentrated in the lower troposphere so the heavy rain location can be easily traced around 925 hPa. Figure 9 shows the horizontal distributions at 850 and 925 hPa. Apparently, the GMPV (Figs. 9a,d) is influenced mostly by the GMPV1 (Figs. 9b,e). Both cover the heavy rain regions well although their areal coverages are a bit too wide, particularly in southwestern and northeastern China. Similar to the MPV2, the GMPV2 (Figs. 9c,f) has the smallest areal coverage among the three with much reduced false alarms, but with many "misses" resulting. For the GMPV, GMPV1, and GMPV2, the performance is better at 925 hPa than at 850 hPa (more misses at 850 hPa by positive PV area). At the same time, all of them cover the heavy rain areas better than do MPV, MPV1, and MPV2 at both levels (cf. Fig. 6). Given the better performance of GMPV, GMPV1, and GMPV2 at 925 hPa, they will be evaluated at 925 hPa hereafter.

To find robust results, GMPV and MPV were systematically compared based on the independent 41 daily regional heavy rain cases from 1998 (Table 1). The threat score [TS; Eq. (8); Palmer and Allen (1949)] is calculated to quantitatively measure how well a parameter overlaps with a heavy precipitation area ($\geq$25 mm day^{-1}) based on all grid points within China on a 0.5° latitude–longitude grid. From Eq. (8), we can see that TS takes missing M and false alarm (FA) values into account besides counting overlapping or hitting areas H:

$$\mathrm{TS} = \frac{H}{\mathrm{FA} + H + M}. \tag{8}$$

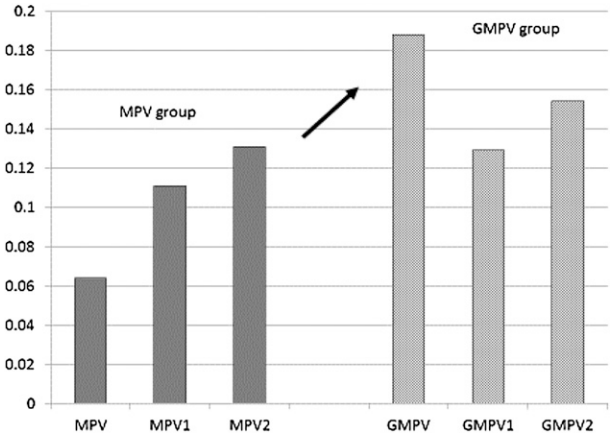

FIG. 11. Average TS of various parameters from the MPV and GMPV groups in depicting the heavy precipitation area ($\geq$25 mm day^{-1}) based on 41 daily heavy rain cases occurring in eastern China during 1998. The TS difference between MPV and GMPV is statistically significant at the 99% level based on the Student's t test.

To be fair to all parameters, an optimal threshold (maximizing the TS for a parameter; Fig. 10) is first determined for each parameter based on the 41-case average; then the optimal threshold is used to define the area of each corresponding parameter like MPV and GMPV, etc. The TS results averaged over the 41 cases are shown in Fig. 11 and Table 2. The improvement found for GMPV over MPV is significant: increases in TS of 194%, 16%, and 18% for GMPV, GMPV1, and GPMV2, respectively. The improvement found in GMPV over MPV is statistically significant at a 99% confidence level based on a Student's t test, while the improvement in GMPV1 (GMPV2) over MPV1 (MPV2) is statistically significant at the 65% (80%) confidence level. The less significant improvement seen for the two components rather than for the total term is consistent with the result of the 1 July 1991 case (e.g., cf. Figs. 5 and 8 or Figs. 6 and 9).

The reason why the GMPV is superior to the MPV is in the more realistic treatment of moisture in the heavy rain area when replacing the equivalent potential temperature with the generalized equivalent potential temperature. To demonstrate this, Figs. 12 and 13 compare the horizontal and vertical distributions and gradients of θ_e and θ^* of the 1 July 1990 case. We can see that horizontally θ^* is more concentrated around the heavy rain areas than is θ_e (Figs. 12 and 13a,b), while vertically the major signal from $\partial\theta^*/\partial p$ is concentrated closer to the lower level than that from $\partial\theta_e/\partial p$ (Figs. 13c,d). This explains why GMPV has stronger signals near the heavy rain area and the lower level than does MPV, as we observed in Figs. 8 and 9 (cf. Figs. 5 and 6). For the total terms (MPV and GMPV), the reason that GMPV is superior is that both GMPV1 and GMPV2 have the same sign so they can be added together to make a more obvious signal (Figs. 8 and 9), while MPV1 and MPV2 are opposite in sign in most areas, smearing the signal (Figs. 5 and 6). This difference stems also from the difference between θ_e and θ^*. For MPV1 [Eq. (5b)] and GMPV1 [Eq. (7b)], they remain of the same sign because both $\partial\theta_e/\partial p$ and $\partial\theta^*/\partial p$ are negative in the lower level over the heavy rain area (Figs. 13c,d) reflecting convective instability. For the MPV2 [Eq. (5c)] and GMPV2 [Eq. (7c)], they have opposite signs because $\partial\theta_e/\partial y$ and $\partial\theta^*/\partial y$ have opposite signs (Figs. 13e,f). The $\partial\theta_e/\partial y$ ($\partial\theta^*/\partial y$) relates more on the heat (moisture) content and is negative (positive) over the heavy rain area. Note that the impact from the zonal gradients

TABLE 2. TS and std dev (with respect to mean) of various parameters in depicting heavy rain locations ($\geq$25 mm day^{-1}) based on 41 daily cases occurring in eastern China in 1998. Here, TS_{mean}, TS_{best}, and TS_{worst} are the mean, best, and worst TS for a parameter. Statistical significance of an improvement is based on a Student's t test. The optimal threshold used for each parameter is also listed based on the 41-case average.

Parameter	Threshold	TS_{mean}	TS_{best} (date)	TS_{worst} (date)	Std dev	Statistical significance
D (850 hPa)						
D	-2.0×10^{-5}	0.169	0.320 (9 Mar)	0.000 (29 Jul)	0.0804	—
MD $\{D[(q/q_s)^{10}]\}$	-0.5×10^{-5}	0.270	0.548 (26 Jun)	0.073 (29 Jul)	0.0868	99% (over D)
ζ (850 hPa)						
ζ	4.3×10^{-5}	0.196	0.384 (2 Jul)	0.010 (8 Mar)	0.0819	—
MV $\{\zeta[(q/q_s)^{10}]\}$	1.4×10^{-5}	0.262	0.498 (26 Jun)	0.121 (16 Feb)	0.0895	99% (over ζ)
MPV (850 hPa)						
MPV	0.03	0.064	0.171 (6 Jul)	0.001 (8 Mar)	0.0370	—
MPV1	0.2	0.111	0.309 (14 Jan)	0.000 (24 Jul)	0.0827	—
MPV2	−0.2	0.131	0.369 (22 Aug)	0.000 (22 Jul)	0.0955	—
GMPV (925 hPa, k = 10)						
GMPV	0.4	0.188	0.382 (23 May)	0.067 (15 Aug)	0.0636	99% (over MPV)
GMPV1	0.2	0.129	0.317 (14 Jan)	0.019 (17 Feb)	0.0713	65% (over MPV1)
GMPV2	0.2	0.154	0.315 (9 Jun)	0.022 (8 Mar)	0.0637	80% (over MPV2)

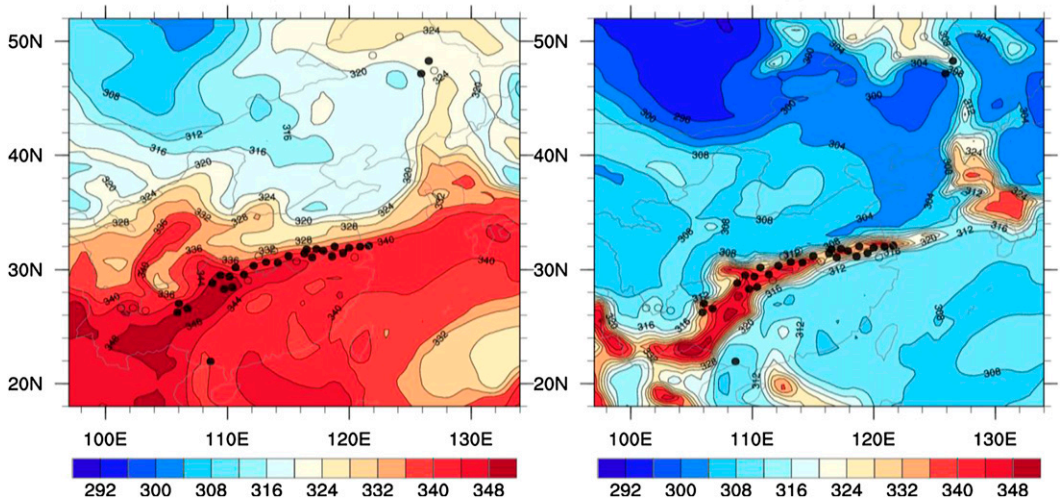

FIG. 12. (left) The equivalent potential temperature and (right) the generalized equivalent potential temperature ($k = 10$) at 850 hPa at 0000 UTC 1 Jul 1991 (K; contours with an interval of 4 K).

$\partial\theta_e/\partial x$ and $\partial\theta^*/\partial x$ should be small as a result of the east–west orientation of both θ_e and θ^* (Fig. 12). Considering the positive vorticity (this factor impacts magnitude but not sign because the absolute vorticity term is always positive), as well as the convectively unstable and vertically increasing zonal wind speed (below the low-level jet) environment a heavy rain event normally has, we would expect to find positive MPV1 and negative MPV2 in MPV, and both positive GMPV 1 and GMPV2 in GMPV based on Eqs. (5b), (5c), (7b), and (7c).

c. *Moist vorticity and moist divergence*

Following the approach used for GMPV, we extend the vorticity [Eq. (1)] and divergence [Eq. (2)] to the moist vorticity [MV; Eq. (9)] and moist divergence [MD; Eq. (10)] by multiplying the same relative humidity–based weight:

$$\mathrm{MV} = \left(\frac{\partial v}{\partial x} - \frac{\partial u}{\partial y}\right)\left(\frac{q}{q_s}\right)^k \quad \text{and} \tag{9}$$

$$\mathrm{MD} = \left(\frac{\partial u}{\partial x} + \frac{\partial v}{\partial y}\right)\left(\frac{q}{q_s}\right)^k, \tag{10}$$

where $k = 0, 1, 2, \ldots$, indicates the relative contribution of moisture. When $k = 0$, moisture has no impact and the MV and MD become the original dry vorticity and divergence, respectively. As in section 3b for GMPV, $k = 10$ is used in MV and MD. To examine if MV and MD improve over the original vorticity and divergence, Fig. 14 shows the latitudinal–vertical cross section through the heavy rainband along 114.75°E at 0000 UTC 1 July 1991, which shows that the signals from both the MV (Fig. 14b) and MD (Fig. 14d) are weaker (less sharper) but more concentrated around the heavy rain area compared to the vorticity (Fig. 14a) and divergence (Fig. 14c), because of the concentrated distribution of the relative humidity–based weight $(q/q_s)^{10}$ (Fig. 7e). For example, the high vorticity in the upper levels and at multiple lower-level centers (near 28°, 37°, and 49°N, where no heavy rain occurred; Fig. 14a) is much reduced or disappears in the MV. Similar improvement is found for the MD over the divergence. This concentration of signal can be more clearly seen in the plain view of the fields (Figs. 15 and 16). Since the maxima of the MV and MD are located around 850 hPa, Figs. 15 and 16 show the horizontal distributions of the MV and MD at 850 hPa at every 6 h during the entire period of the 1 July 1991 heavy rain event. The improvement of a dynamic–moisture combined parameter (MV and MD) is obvious over either a dynamic-only parameter (vorticity and divergence) or a moisture-only parameter (relative humidity): for example, the spurious areal coverage in northwestern China indicated by the original vorticity (Fig. 2) and divergence (Fig. 3) has now disappeared and the spurious areal coverage in southwestern China indicated by the original humidity field (Fig. 4) has also been eliminated, while the heavy rainband along the Yangtze River is well indicated by both MV and MD. This is true for all five of the time points during the event. In addition, other globally observed precipitation datasets (not shown) indicated that the maximum center located at the southern tip of the Korean Peninsula, as shown for both MV and MD, does overlap with an area of heavy rain events although no observations of heavy rain are marked in the plot because of its location outside of China.

As in section 3b, TS is again calculated based on the 41 daily regional heavy rain cases to quantitatively measure

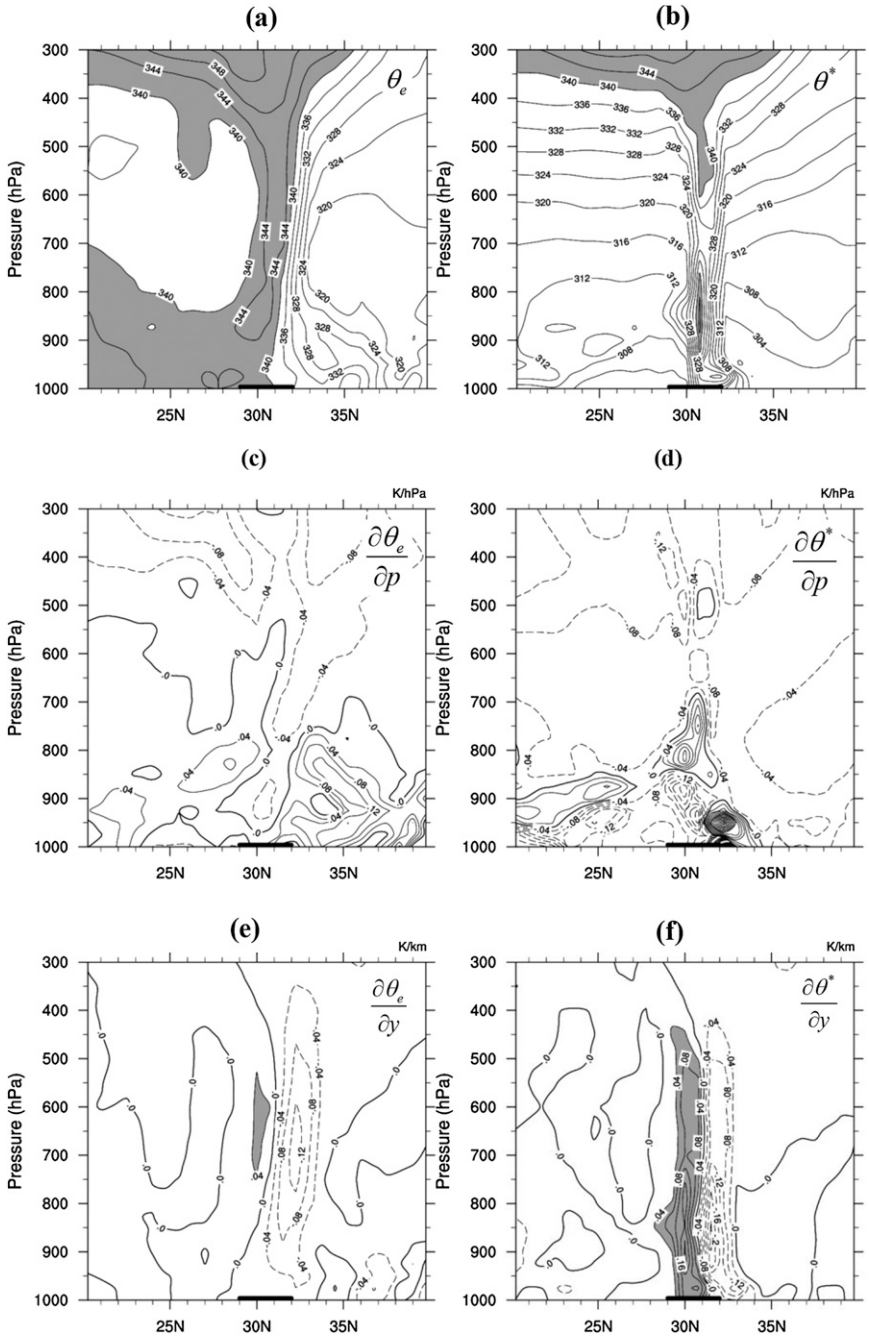

FIG. 13. Vertical–latitude cross sections of (a) the equivalent potential temperature (K; contours with an interval of 4 K), (b) the generalized equivalent potential temperature (K; contours with an interval of 4 K), (c) the vertical gradient of θ_e (K hPa^{-1}; contours with an interval 0.04 K hPa^{-1}), (d) the vertical gradient of θ^* (K hPa^{-1}; contours with an interval 0.04 K hPa^{-1}), (e) the horizontal gradient (from south to north) of θ_e (K km^{-1}; contours with an interval of 0.04 K km^{-1}), and (f) the horizontal gradient of θ^* (K km^{-1}; contours with an interval of 0.04 K km^{-1}), along 114.75°E at 0000 UTC 1 Jul 1991. The heavy rainband is highlighted by the heavy solid line.

how well a vorticity- or a divergence-related parameter overlaps with a heavy precipitation area (≥25 mm day^{-1}) within China. Similar to the situations for vorticity and divergence in Figs. 2 and 3, although the MV and MD are similar to each other in general at different times during the event, the midpoint 0000 UTC (Figs. 15c, 16c) seems to match the heavy rain area the best (at least as well as others). Therefore, the midpoint is again used as a

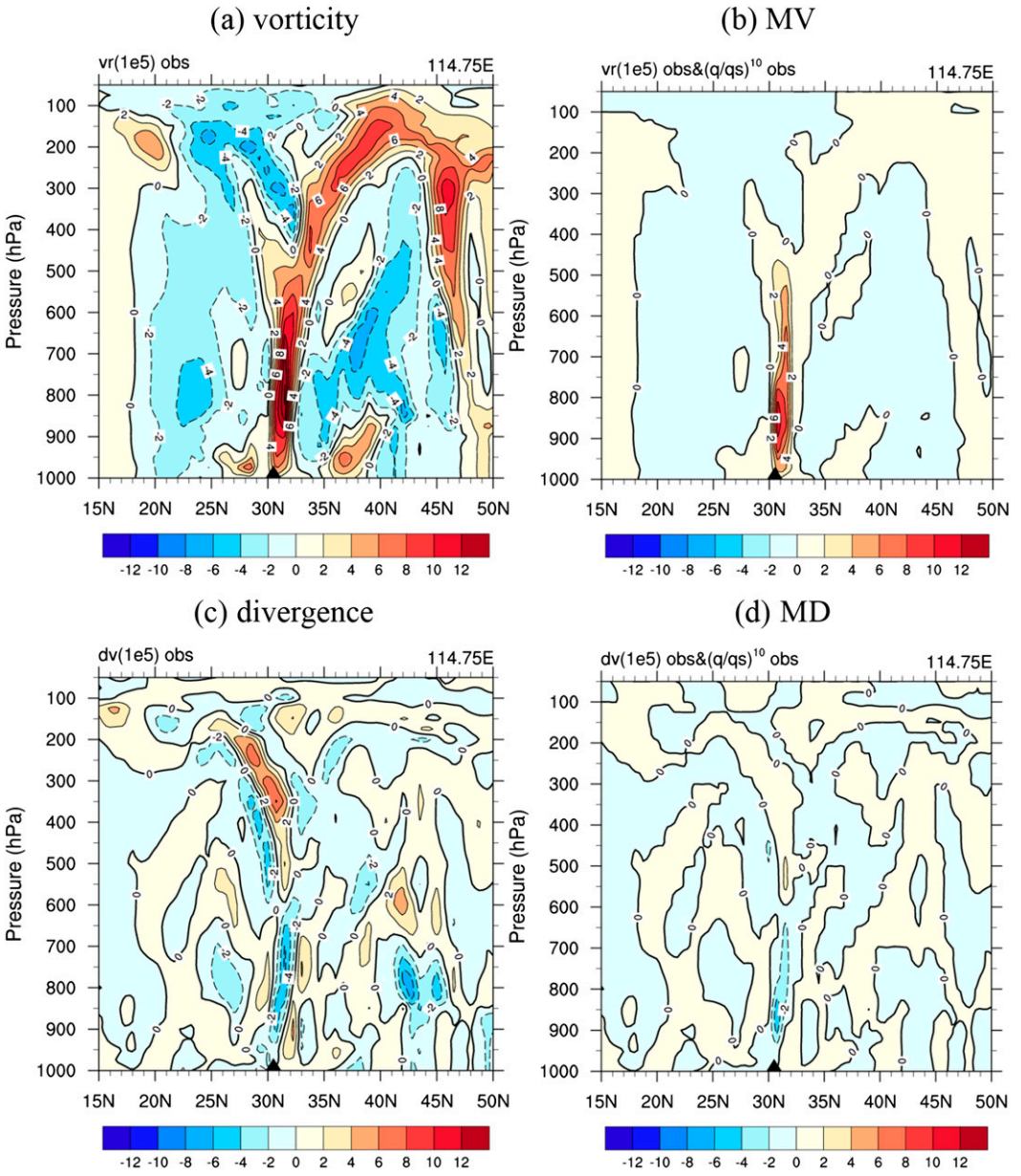

FIG. 14. Vertical–latitude cross sections (s^{-1}; contours with an interval of $2 \times 10^{-5}\,s^{-1}$) of (a) vorticity, (b) MV, (c) divergence, and (d) MD at 0000 UTC 1 Jul 1991. The heavy rain area is indicated by the filled triangles.

representative time for a daily regional heavy rain event in the following statistics. The optimal threshold for each parameter is shown in Fig. 17. Based on these optimal thresholds, Fig. 18 shows the averaged TS results for the three groups (note the MPV vs GMPV group is the same as in Fig. 11 and is listed for comparison purposes). After incorporating the effects of moisture into the vorticity and divergence, the improvements of MV or MD over the vorticity or divergence are significant: about a 60% increase in TS for MD (from 0.169 to 0.27) and 24% for MV (from 0.196 to 0.262). This result is also statistically significant at the 99% confidence level. The averaged TS as well as the best and worst scores and their variance (standard deviation with respect to mean) for each parameter out of the 41 cases are also listed in Table 2 along with the statistical significance levels.

4. Conclusions and discussion

Heavy precipitation is an outcome of combined favorable dynamic and moisture conditions. Our study demonstrated that a parameter containing either a

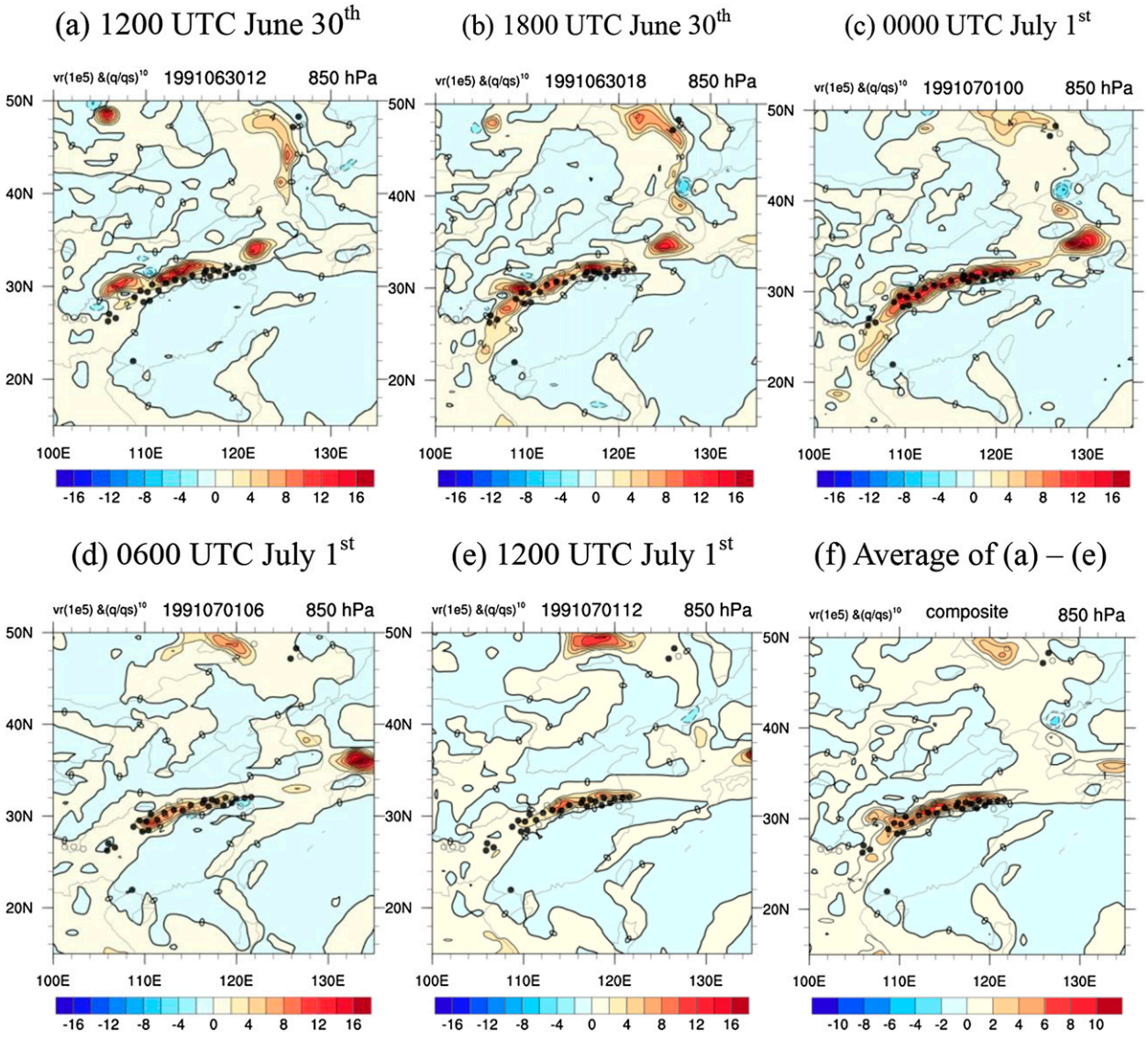

FIG. 15. As in Fig. 2, but for MV ($k = 10$).

dynamic or moisture factor alone, such as vorticity, divergence, or relative humidity, cannot accurately depict heavy rain areas (often leading to too many false alarms), but properly including moisture effects into a dynamical parameter can significantly increase a parameter's ability to diagnose heavy rain locations. In this study, a regional heavy rain event that occurred along the Yangtze River on 1 July 1991 is used as a case study, and another 41 daily regional heavy rain events during the notorious flooding year of 1998 in eastern China are used for systematic evaluation. TS is used to quantitatively measure the overlap between a parameter and the heavy rain areas. Because of the limited spatial resolution (~80 km) of the reanalysis data, only long-lasting large-scale widespread regional heavy rain events associated with synoptic-scale weather systems are investigated.

Although the GMPV was proposed about 10 years ago (Gao et al. 2004a), it is still unfamiliar to many. Therefore, the concept of GMPV is introduced first. The empirical relative humidity–based weighting approach used to modify the effects of moisture in the MPV to become a GMPV is then analyzed. It is found that the GMPV is superior to the MPV in depicting heavy rain locations; for example, GMPV can increase TS by 194% over the MPV on average (increasing from 0.064 to 0.188), which is statistically significant at the 99% confidence level. The two components of the MPV are also

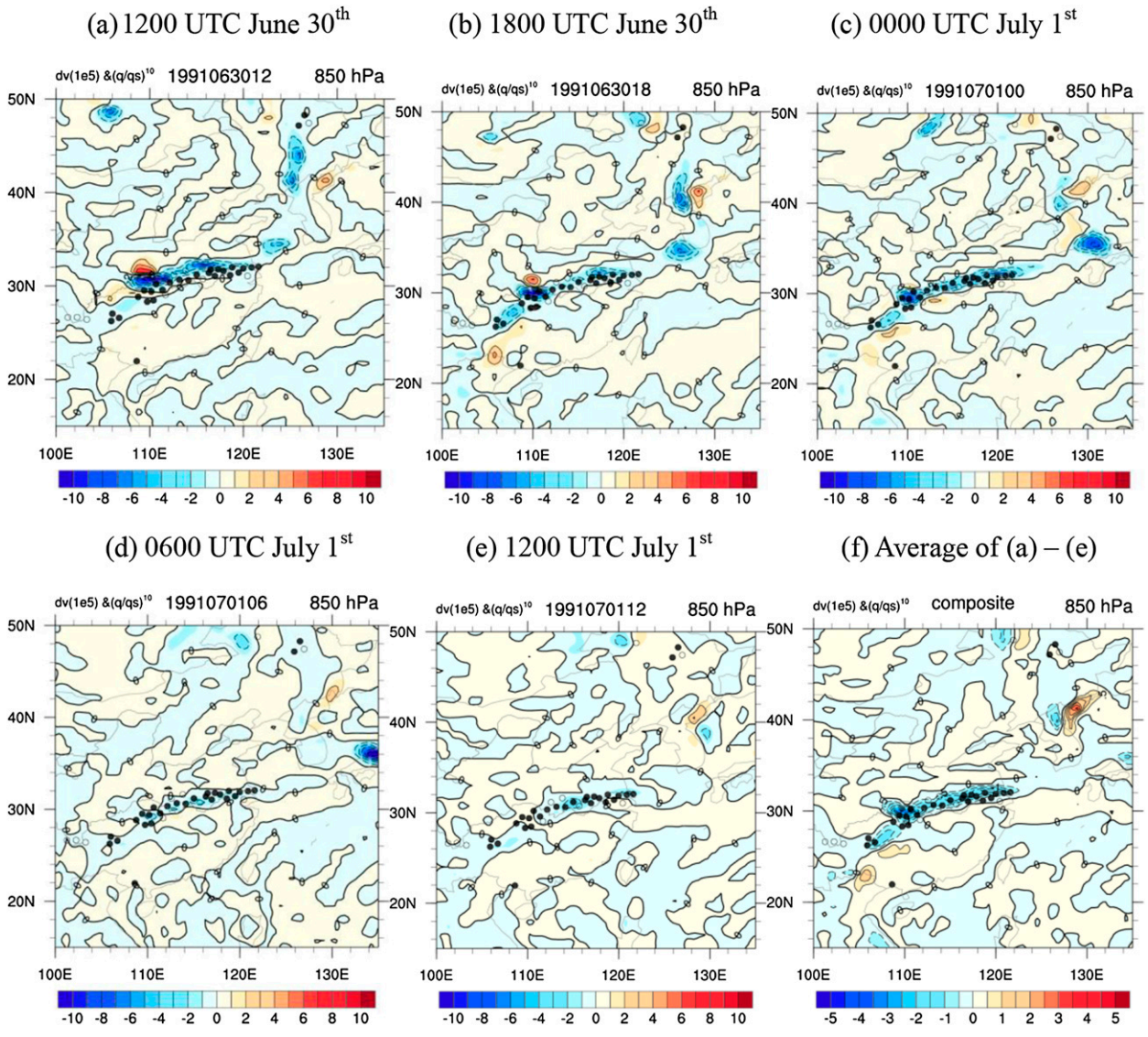

FIG. 16. As in Fig. 3, but for MD (k = 10).

improved by those of the GMPV: a 16% increase in TS for the GMPV1 over the MPV1 (from 0.111 to 0.129), and 18% for the GMPV2 over the MPV2 (from 0.131 to 0.154), results that are statistically significant at the 65% and 80% confidence levels, respectively.

Following the same empirical relative humidity–based weighting approach, two new diagnostic parameters (MV and MD) are proposed for the first time by incorporating moisture effects into the traditional vorticity and divergence. Results show that after the moisture effects are properly incorporated, the improved ability of the vorticity and divergence to capture heavy rain areas is significant. For example, MV is superior to the vorticity by 24% (from 0.196 to 0.262), and MD to the divergence by 60% (from 0.169 to 0.27) in terms of TS, averaged over the 41 cases. Many spurious areas are eliminated. These improvements are statistically significant at the 99% confidence level. Both MV and MD are superior to GMPV in depicting heavy rain locations. Although MV and MD perform similarly to each other on average, the performance of MV seems to be more stable than that of MD. For example, the range in TS variation is narrower for MV (from 0.121 to 0.498) than for MD (from 0.073 to 0.548).

Although application of MV and MD in assessing heavy rain potential is not intended to replace a complete, multiscale forecasting methodology, such as that of Doswell et al. (1996), the two new parameters could be used to postprocess a model forecast to potentially improve heavy rain location predictions in the following

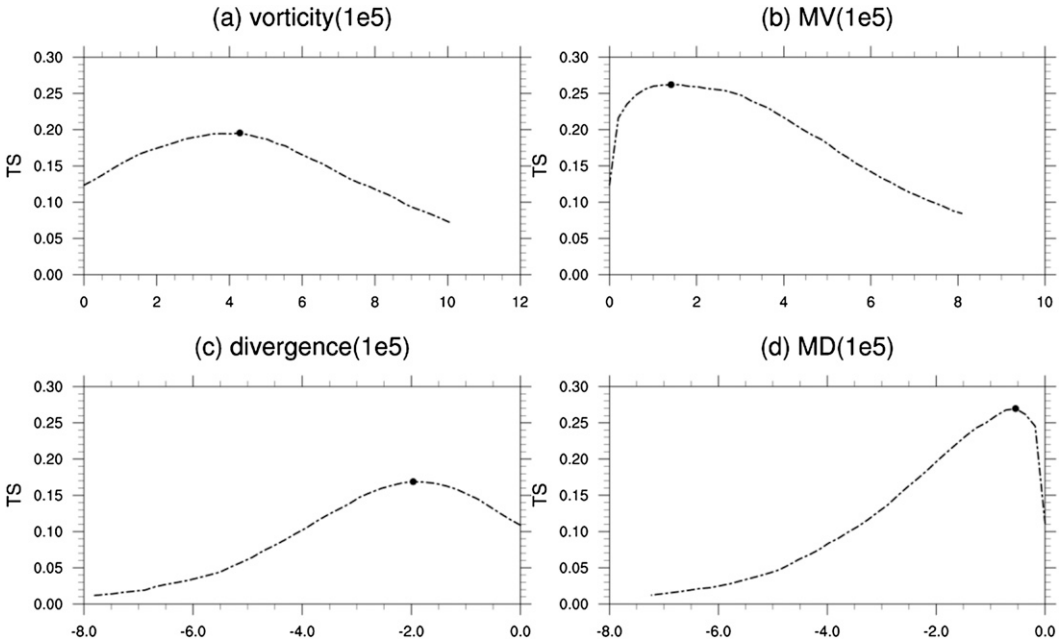

FIG. 17. As in Fig. 10, but for (a) vorticity, (b) MV, (c) divergence, and (d) MD.

three possible ways. First, they could be directly applied to numerical weather prediction model outputs. Since the performance levels of the analysis-based MV and MD (TS = 0.26 and 0.27, respectively) are similar to that of the current operational day-1 forecasts of 24-h accumulated precipitation exceeding 25–50 mm at NCEP, which is about 0.20–0.30 (NCEP/WPC 2014), it might be hard to add value over short-range (1–2 days) heavy rain forecasts. However, it could be valuable for longer-range (beyond a few days) forecasts given the fact that atmospheric circulation (wind, temperature, humidity, and pressure) is more predictable than precipitation. If their application is further combined with ensemble forecasts (Du et al. 1997), the performance of MV and MD could be even more reliable and extended to longer forecast ranges. Second, they could be used to replace the conventional vorticity and divergence in model's statistical postprocessing such as model output statistics (Glahn and Lowry 1972) and other machine-learning schemes. Third, they could be used to calibrate model forecasts such as physically based bias and displacement error correction to greatly improve heavy rain prediction (Du et al. 2000). At the same time, it will also be necessary to further examine how the performance of MV and MD varies with weather systems (such as smaller-scale convection) and for different geographical regions. Our final hope is that the approach of combining dynamic and moisture factors together as demonstrated in this study could inspire similar works in the future to advance our understanding of atmospheric behavior and improve diagnostic and prediction tools.

Acknowledgments. The authors wish to thank the editors and anonymous reviewers for their valuable comments and suggestions to improve the paper. This work is supported by the National Natural Science Foundation of China (41375073), the Strategic Priority Research Program of the Chinese Academy of Sciences (XDA0509400), and the Key Technologies R&D Program (201306032). Ms. Mary Hart of NCEP is appreciated for her help in improving the readability of the manuscript.

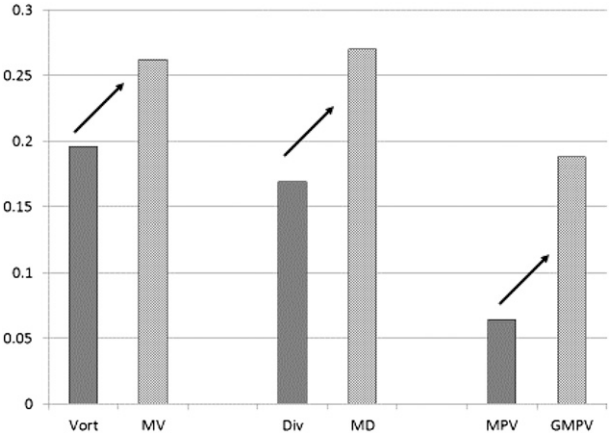

FIG. 18. As in Fig. 11, but for vorticity vs MV and divergence vs MD (MPV vs GMPV is taken from Fig. 11).

REFERENCES

Bennetts, D. A., and B. J. Hoskins, 1979: Conditional symmetric instability—A possible explanation for frontal rainbands. *Quart. J. Roy. Meteor. Soc.*, **105**, 945–962, doi:10.1002/qj.49710544615.

——, and J. C. Sharp, 1982: The relevance of conditional symmetric instability to the prediction of mesoscale frontal rainbands. *Quart. J. Roy. Meteor. Soc.*, **108**, 595–602, doi:10.1002/qj.49710845707.

Cao, Z., and H.-R. Cho, 1995: Generation of moist potential vorticity in extratropical cyclones. *J. Atmos. Sci.*, **52**, 3263–3281, doi:10.1175/1520-0469(1995)052<3263:GOMPVI>2.0.CO;2.

Chen, D., T. Ou, L. Gong, C. Y. Xu, W. Li, C. H. Ho, and W. Qian, 2010: Spatial interpolation of daily precipitation in China: 1951–2005. *Adv. Atmos. Sci.*, **27**, 1221–1232, doi:10.1007/s00376-010-9151-y.

Clark, J. H. E., R. P. James, and R. H. Grumm, 2002: A re-examination of the mechanisms responsible for banded precipitation. *Mon. Wea. Rev.*, **130**, 3074–3086, doi:10.1175/1520-0493(2002)130<3074:AROTMR>2.0.CO;2.

Dee, D. P., and Coauthors, 2011: The ERA-Interim reanalysis: Configuration and performance of the data assimilation system. *Quart. J. Roy. Meteor. Soc.*, **137**, 553–597, doi:10.1002/qj.828.

Deng, G., and S. T. Gao, 2009: The theory of moist potential vorticity and its application in the diagnosis of typhoon rainfall and intensity. *J. Trop. Meteor.*, **15**, 204–209.

Ding, Y., 1993: *Research on the 1991 Persistent, Severe Flood over Yangtze–Huai River Valley* (in Chinese). Chinese Meteorological Press, 255 pp.

Doswell, C. A., III, H. E. Brooks, and R. A. Maddox, 1996: Flash flood forecasting: An ingredients-based methodology. *Wea. Forecasting*, **11**, 560–581, doi:10.1175/1520-0434(1996)011<0560:FFFAIB>2.0.CO;2.

Du, J., S. L. Mullen, and F. Sanders, 1997: Short-range ensemble forecasting of quantitative precipitation. *Mon. Wea. Rev.*, **125**, 2427–2459, doi:10.1175/1520-0493(1997)125<2427:SREFOQ>2.0.CO;2.

——, ——, and ——, 2000: Removal of distortion error from an ensemble forecast. *Mon. Wea. Rev.*, **128**, 3347–3351, doi:10.1175/1520-0493(2000)128<3347:RODEFA>2.0.CO;2.

Emanuel, K. A., 1983: The Lagrangian parcel dynamics of moist symmetric instability. *J. Atmos. Sci.*, **40**, 2368–2376, doi:10.1175/1520-0469(1983)040<2368:TLPDOM>2.0.CO;2.

——, 1988: Observational evidence of slantwise convective adjustment. *Mon. Wea. Rev.*, **116**, 1805–1816, doi:10.1175/1520-0493(1988)116<1805:OEOSCA>2.0.CO;2.

Gao, S. T., T. Lei, and Y. S. Zhou, 2002: Diagnostic analysis of moist potential vorticity anomaly in torrential rain systems (in Chinese). *Quart. J. Appl. Meteor.*, **13**, 662–670.

——, X. R. Wang, and Y. S. Zhou, 2004a: Generation of generalized moist potential vorticity in a frictionless and moist adiabatic flow. *Geophys. Res. Lett.*, **31**, L12113, doi:10.1029/2003GL019152.

——, Y. S. Zhou, X. P. Cui, and G. P. Dai, 2004b: Impacts of cloud-induced mass forcing on the development of moist potential vorticity anomaly during torrential rains. *Adv. Atmos. Sci.*, **21**, 923–927, doi:10.1007/BF02915594.

Glahn, H. R., and D. Lowry, 1972: The use of model output statistics in objective weather forecasting. *J. Appl. Meteor.*, **11**, 1203–1211, doi:10.1175/1520-0450(1972)011<1203:TUOMOS>2.0.CO;2.

Haines, D. A., 1988: A lower atmospheric severity index for wildland fire. *Natl. Wea. Dig.*, **13** (2), 23–27.

Hurrell, J. W., 1995: Decadal trends in the North Atlantic Oscillation: Regional temperatures and precipitation. *Science*, **269**, 676–679, doi:10.1126/science.269.5224.676.

Kiladis, G. N., J. Dias, K. H. Straub, M. C. Wheeler, S. N. Tulich, K. Kikuchi, K. M. Weickmann, and M. J. Ventrice, 2014: A comparison of OLR and circulation-based indices for tracking the MJO. *Mon. Wea. Rev.*, **142**, 1697–1715, doi:10.1175/MWR-D-13-00301.1.

Korty, R. L., and T. Schneider, 2007: A climatology of the tropospheric thermal stratification using saturation potential vorticity. *J. Climate*, **20**, 5977–5991, doi:10.1175/2007JCLI1788.1.

Martínez-Alvarado, O., F. Weidle, and S. L. Gray, 2010: Sting jets in simulations of a real cyclone by two mesoscale models. *Mon. Wea. Rev.*, **138**, 4054–4075, doi:10.1175/2010MWR3290.1.

Moncrieff, M. W., and M. J. Miller, 1976: The dynamics and simulation of tropical cumulonimbus and squall lines. *Quart. J. Roy. Meteor. Soc.*, **102**, 373–394, doi:10.1002/qj.49710243208.

National Climate Center of China, 1998: *The Catastrophic Flood in China in 1998 and Climate Abnormality*. China Meteorological Press, 139 pp.

NCEP/WPC, 2014: Quantitative precipitation forecasts. National Centers for Environmental Prediction/Weather Prediction Center. [Available online at http://www.wpc.ncep.noaa.gov/html/hpcverif.shtml#qpf.]

Novak, D. R., A. C. Brian, and R. McTaggart-Cowan, 2009: The role of moist processes in the formation and evolution of mesoscale snowbands within the comma head of Northeast U.S. cyclones. *Mon. Wea. Rev.*, **137**, 2662–2686, doi:10.1175/2009MWR2874.1.

Palmer, W. C., and R. A. Allen, 1949: Note on the accuracy of forecasts concerning the rain problem. U.S. Weather Bureau, 4 pp.

Qian, W. H., 2013: *Atlas of Anomalous Circulations Associated with Regional Heavy Rainfall in China.* China Meteorological Press, 227 pp.

Schubert, H. W., S. A. Hausman, M. Garcia, K. V. Ooyama, and H. Kuo, 2001: Potential vorticity in a moist atmosphere. *J. Atmos. Sci.*, **58**, 3148–3157, doi:10.1175/1520-0469(2001)058<3148:PVIAMA>2.0.CO;2.

Schultz, D. M., and P. N. Schumacher, 1999: The use and misuse of conditional symmetric instability. *Mon. Wea. Rev.*, **127**, 2709–2732, doi:10.1175/1520-0493(1999)127<2709:TUAMOC>2.0.CO;2.

Shou, S. W., and Y. H. Li, 1999: Study on moist potential vorticity and symmetric instability during a heavy rain event occurred in the Jiang-Huai Valley. *Adv. Atmos. Sci.*, **16**, 314–321, doi:10.1007/BF02973091.

Ventrice, M. J., M. C. Wheeler, H. H. Hendon, C. J. Schreck III, C. D. Thorncroft, and G. N. Kiladis, 2013: A modified multivariate Madden–Julian oscillation index using velocity potential. *Mon. Wea. Rev.*, **141**, 4197–4120, doi:10.1175/MWR-D-12-00327.1.

Wang, B., and Z. Fan, 1999: Choice of South Asian summer monsoon indices. *Bull. Amer. Meteor. Soc.*, **80**, 629–638, doi:10.1175/1520-0477(1999)080<0629:COSASM>2.0.CO;2.

Wolter, K., and M. S. Timlin, 1993: Monitoring ENSO in COADS with a seasonally adjusted principal component index. *Proc. 17th Climate Diagnostics Workshop*, Norman, OK, NOAA/NMC/CAC, 52–57.

Wu, G., Y. Cao, and X. Tang, 1995: Moist potential vorticity and slantwise vorticity development (in Chinese). *Acta Meteor. Sin.*, **53**, 387–405.

Zhou, B., and J. Du, 2010: Fog prediction from a multimodel mesoscale ensemble prediction system. *Wea. Forecasting*, **25**, 303–320, doi:10.1175/2009WAF2222289.1.

Zhou, G. B., C. G. Cui, and S. T. Gao, 2010: Application of generalized moist potential vorticity to the analysis of a torrential rain case. *J. Meteor. Res.*, **24**, 732–739.